

Mechanisms of pore formation in hydrogel scaffolds textured by freeze-drying

Jérôme Grenier, Hervé Duval, Fabrice Barou, Pin Lu, Bertrand David, Didier Letourneur

▶ **To cite this version:**

Jérôme Grenier, Hervé Duval, Fabrice Barou, Pin Lu, Bertrand David, et al.. Mechanisms of pore formation in hydrogel scaffolds textured by freeze-drying. Acta Biomaterialia, 2019, 94, pp.195-203. 10.1016/j.actbio.2019.05.070 . hal-02144830

HAL Id: hal-02144830
https://hal.science/hal-02144830

Submitted on 27 May 2020

HAL is a multi-disciplinary open access archive for the deposit and dissemination of scientific research documents, whether they are published or not. The documents may come from teaching and research institutions in France or abroad, or from public or private research centers.

L'archive ouverte pluridisciplinaire **HAL**, est destinée au dépôt et à la diffusion de documents scientifiques de niveau recherche, publiés ou non, émanant des établissements d'enseignement et de recherche français ou étrangers, des laboratoires publics ou privés.

Mechanisms of pore formation in hydrogel scaffold textured by freeze-drying

Jérôme Grenier [a, b, c], Hervé Duval [a, *], Fabrice Barou [d], Pin Lv [e], Bertrand David [b, 1] and Didier Letourneur [c, 1]

[a] Laboratoire LGPM, CentraleSupélec, Université Paris-Saclay, Gif-sur-Yvette, 91190, France

[b] Laboratoire MSSMat, UMR 8579 - CentraleSupélec, Université Paris-Saclay, Gif-sur-Yvette, 91190, France

[c] Université de Paris, Université Paris 13, INSERM 1148, LVTS, Hôpital Bichat, F-75018 Paris, France

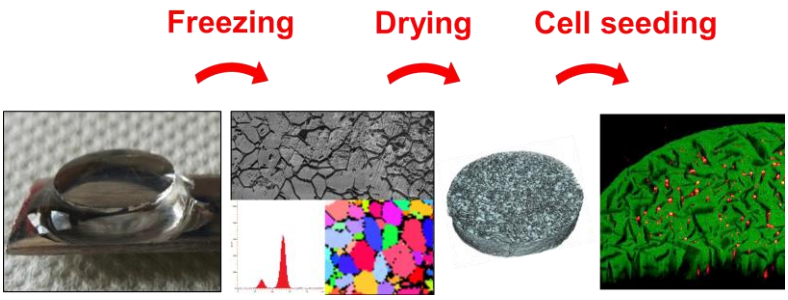
[d] Géosciences Montpellier, UMR 5243, Université Montpellier, CNRS, Montpellier Cedex 05, 34095, France

[e] LGPM, CentraleSupélec, SFR Condorcet FR CNRS 3417, Université Paris-Saclay, Centre Européen de Biotechnologie et de Bioéconomie (CEBB), 3 rue des Rouges Terres 51110 Pomacle, France

[*] Corresponding author: herve.duval@centralesupelec.fr

[1] equal last authors

Graphical Abstract



Keywords

Polysaccharide-based hydrogel; Ice-templating; Freeze-drying; Porous scaffolds; 3D cell culture

Statement of significance

The fabrication of hydrogel scaffolds is an important research area in tissue engineering. Hydrogels are textured to provide a 3D-framework that is favorable for cell proliferation and/or differentiation. Optimum hydrogel pore size depends on its biological application. Producing porous hydrogels is commonly achieved through freeze-drying. However, the mechanisms of pore formation remain to be fully understood. We carefully analyzed scaffolds of a cross-linked polysaccharide-based hydrogel developed for bone tissue engineering, using state-of-the-art microscopic techniques. Our experimental results evidenced the shaping of hydrogel during the freezing step, through a specific ice-templating mechanism. These findings will guide the strategies for controlling the porous structure of hydrogel scaffolds.

Abstract

Whereas freeze-drying is a widely used method to produce porous hydrogel scaffolds, the mechanisms of pore formation involved in this process remained poorly characterized. To explore this, we focused on a cross-linked polysaccharide-based hydrogel developed for bone tissue engineering. Scaffolds were first swollen in 0.025% NaCl then freeze-dried at low cooling rate, i.e. - 0.1 °C min^{-1}, and finally swollen in aqueous solvents of increasing ionic strength. We found that scaffold's porous structure is strongly conditioned by the nucleation of ice. Electron cryo-microscopy of frozen scaffolds demonstrates that each pore results from the growth of one to a few ice grains. Most crystals were formed by secondary nucleation since very few nucleating sites were initially present in each scaffold (0.1 nuclei cm^{-3} $°C^{-1}$). The polymer chains are rejected in the intergranular space and form a macro-network. Its characteristic length scale coincides with the ice grain size (160 µm) and is several orders of magnitude greater than the mesh size (90 nm) of the cross-linked network. After sublimation, the ice grains are replaced by macro-pores of 280 µm mean size and the resulting dry structure is highly porous, i.e. 93%, as measured by high-resolution X-ray tomography. In the swollen state, the scaffold mean pore size decreases in solvent of increasing ionic strength (120 µm in 0.025% NaCl and 54 µm in DBPS) but the porosity remains the same, i.e. 29% regardless of the solvent. Finally, cell seeding of dried scaffolds demonstrates that the pores are adequately interconnected to allow homogenous cell distribution.

1. Introduction

Biocompatible hydrogel scaffolds have recently gained increasing interest in tissue engineering [1], with manufacturing suitable scaffolds for cell culture and tissue regeneration remaining an intensive area of development since the early 80s [2]. Cell attachment, viability [3] and migration [4] are strongly correlated with pore size. Porous matrix can be produced by various methods such as fiber bonding, salt leaching, foaming and 3D printing [5]. Freeze-drying (**Fig. 2**) is a versatile method for producing porous hydrogels [6]. Two manufacturing routes are reported in the literature: (1) a polymeric solution is cross-linked and then freeze-dried, or (2) a polymeric solution is freeze-dried and then cross-linked or coprecipitate [7]. Whatever the route, the final texture strongly depends on the cooling rate during the cooling step. During this stage, the free water and possibly part of the bound water transform into ice [8]. This phase transition is referred to as freezing or solidification. In the case of low cooling rate, equiaxed solidification of water leads to 3D homogenous structure [9]. Quenching in liquid nitrogen [10], or unidirectional freezing technologies [11–13], on the contrary, favor columnar solidification of water leading to 2D ordered tubular structure with aligned channel pores, which has an average spacing that is dependent on the cooling rate. However, quenching in liquid nitrogen or unidirectional freezing are less scalable than standard freeze-drying at a low cooling rate.

Water solidification within hydrogel takes place in two stages, *i.e.*, nucleation in supercooled water followed by ice growth at a temperature near the ice melting point (**Fig. 2**). Ice acts as a porogen. This process called the ice-templating has been primarily studied for colloid suspensions [14], but to a much lesser extent for polymer hydrogels. Since the polymer solubility is lower in ice than in liquid water, the polymer chains are rejected by the growing ice crystals and then form a continuous macro-network or super-network that interpenetrates the ice network on the ice grain scale [15]. The term “grain” refers to a crystal surrounded by

other crystals and implies the existence of grain boundaries that hold the grains together. For clarification, the use of the more general term “crystal” is here restricted to isolated crystals.

The scenario described above has been first advanced for the Manufacturing Route 2 but never evidenced. Furthermore, its relevance for Route 1 is not straightforward since the polymer is cross-linked before the freezing step.

To explain how water solidification conditioned the application properties of cross-linked hydrogels, we raised the following issues: First, the ice network and the segregation of the polymer chains on the ice grain boundary network have never been observed. Second, the characterization of the porous structure is most often carried out in 2D which gives a biased interpretation [12]. Last, the use of the dried structure in cell culture conditions needs to be further examined. In this work, we address the mechanisms of pore formation by freeze-drying in a polysaccharide-based hydrogel scaffold designed for bone tissue engineering [16]. This biomaterial is under research and industrial developments [17–21]. The scaffolds are manufactured according to Route 1 with a low cooling rate. For the first time, the sketch of water solidification within the hydrogel scaffold was revealed by Electron Backscattering Diffraction (EBSD) coupled with Energy-Dispersive X-ray spectroscopy (EDX) at -100°C. EBSD is a very powerful technique for the characterization of crystalline microstructures in the scanning electron microscope. It can provide accurate and quantitative data to analyze microstructure of the materials, e.g. sizes and morphology of individual grains, crystal orientation… The technique can now be used to analyzing ice at -100°C [22,23]. After freeze-drying, the porous structure of the scaffolds was analyzed in its entirety in 3D with high-resolution microscopy (X-ray tomography). The porous structure in cell culture conditions was then investigated with Confocal Laser Scanning Microscopy (CLSM). Finally, an in-depth analysis of the experimental results provided a clear picture of the mechanisms underlying the

formation and the evolution of pores within cross-linked hydrogel scaffold. These findings will help to control and optimize the porous structure of hydrogel scaffold.

2. Materials and methods

2.1 Polysaccharides

Pullulan 200 kDa (Hayashibara, Okayama, Japan) and dextran 500 kDa (Pharmacosmos, Holbaek, Denmark) were used in this study. Solutions of pullulan or dextran (10 g L^{-1}) in $NaNO_3$ (0.15 mol L^{-1}) were analyzed using size exclusion chromatography with HPLC equipped with PWxl Guard-column (TSK-GEL®) operated at 0.5 mL min^{-1}. Number and mass average molecular weights (resp. M_n and M_w), polydispersity (I_p) and gyration radius (R_n) were computed with light scattering instrument TREOS (Wyatt Technology) using 0.14 mL g^{-1} refractive-index increment and 657 nm wavelength.

2.2 Hydrogel formulation

The polysaccharide-based hydrogel was synthesized with an aqueous solution of polysaccharides (75% pullulan – 25 % dextran (w/w), 0.3 g mL^{-1}) containing NaCl (0.35 g mL^{-1}) according to published protocols [16,24]. Sodium trimetaphosphate (STMP) solution (0.3 g mL^{-1}) was added under alkaline conditions obtained after the addition of NaOH solution (10 mol L^{-1}). Final solution contained 16.5 % g-STMP g-polysaccharides $^{-1}$. The solution was rapidly cast between glass plates with a 1 mm gap and placed for 20 minutes at 50 °C in an oven (**Fig. 1**). Scaffolds were formed by disc-cutting (Harris Uni-Core, Sigma Aldrich) at 5 mm in diameter. Scaffolds were then neutralized with Phosphate Buffer Saline solution (10x) and extensively washed with 0.025 % (g L^{-1}) NaCl solution until equilibrium at 540 µS cm^{-1}. Since hydrogel scaffolds were cast in the shape of a cylinder, we use, in the whole text, X and Y for designating the directions parallel to the cylinder base and Z for its symmetry axis.

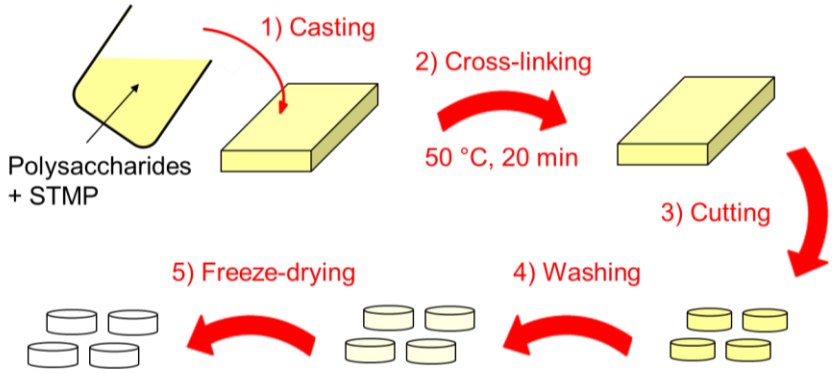


Fig. 1. Schematic illustration of the scaffold fabrication process.

2.3 Swelling experiments

The volume fraction of the polymer in the relaxed state (v_{2r}) and in the swollen state (v_{2s}) was determined by weighing the hydrogel in the relaxed state (W_r) and in the swollen state (W_s). The polymer dried weight (W_d) was obtained after extensive washing in pure water and 4 days at 50°C in a low vacuum chamber.

As a first approximation, we neglected the concentration dependence of the partial specific volumes of water and polymer and assumed that the hydrogel behaves as an infinitely dilute system. The partial specific volume of the polymer mixture (v) was estimated at 0.0006125 m^3 kg^{-1} by mass-averaging the partial specific volumes of dextran and pullulan at infinite dilution [25,26]. The partial specific volume of the solvent was taken equal to the specific volume of the pure solvent. Then, the volume fractions of the polymer read

$$v_{2r,s} = \frac{W_d\, v}{\left((W_{r,s} - W_d)/\rho_{r,s}\right) + W_d\, v} \quad (1)$$

where ρ_r is the density of the solvent associated with the relaxed state, i.e. the solvent used for cross-linking, and ρ_s is the density of the solvent associated with the swollen state of the polymer. The swelling volume ratio is defined as $Q = 1/v_2 s$

148

149 2.4 **Rheological measurements and mesh size**

150 Scaffolds (2 cm in diameter) were analyzed with Discovery HR-2 (TA Instrument®) rheometer
151 between plan-plan crosshatched geometry. Immersion cup and Peltier plates allowed
152 equilibrium at 37°C with 0.025 % NaCl. Axial force standardization was achieved by
153 monitoring axial force against gap reduction until surface leap effect have been overcome [27].
154 The storage modulus of the hydrogel (*G'*) was determined from the characterization of six
155 independent samples with no more than 0.1 N axial force at 0.05 % strain (linear domain) and
156 1 Hz oscillation. The number average molecular weight between cross-links (M_c) was deduced
157 from the storage modulus using the Gaussian rubber elasticity theory modified by Peppas and
158 Merrill [28,29]:

$$G = \frac{\mathrm{R\,T}\,C_{2r}}{M_c}\left(1 - \frac{2M_c}{M_n}\right)\left(\frac{v_{2r}}{v_{2s}}\right)^{-\frac{1}{3}} \quad (2)$$

159 where R is the gas constant (J mol^{-1} K^{-1}), C_{2r} is the polymer concentration in the relaxed state
160 (kg m^{-3}) and M_n is the number average molecular weight of pullulan – dextran mixture.
161 Equation (2) is valid if the polymer network behaves as a collection of Gaussian chains.
162 According to Treloar [28], the regime is Gaussian as long as the relative end-to-end distance
163 of the network chains remains lower than 0.3. We checked that this condition was actually met
164 (see the Results section).

165 Since there is no model of end-to-end distance for chains made of both pullulan and dextran,
166 the end-to-end distance of the chains in the unperturbed state, $\left(\overline{r_0^2}\right)^{\frac{1}{2}}$, was estimated under 100%
167 pullulan and 100% dextran assumption. Furthermore, we neglected the effect of the
168 monolinked phosphate on the end to end distance. The number average molecular weight
169 between cross-links under 100% pullulan (resp. dextran) assumption, denoted M_c^{pul} (resp.

M_c^{dex}), was thus calculated from equation (2) with M_n^{pul} (resp. M_n^{dex}). Then, the end-to-end distance was estimated for pullulan following: $\left(\overline{r_0^2}\right)^{\frac{1}{2}} \cong l\left(\left(M_c^{pul}/M_r\right)C_\infty\right)^{\frac{1}{2}}$ with alpha-D-glucose residue as repeating unit (M_r = 162 g mol^{-1}), l = 4.79 Å and C_∞ = 4.3 according to Buliga and Brant [30]. For dextran, the end-to-end distance was computed following: $\left(\overline{r_0^2}\right)^{\frac{1}{2}} = 0.071\sqrt{M_c^{dex}}$ according to İmren et al. [25]. The mesh size in the swollen state was estimated for dextran chains and pullulan chains with equation (3) according to Canal and Peppas [31]:

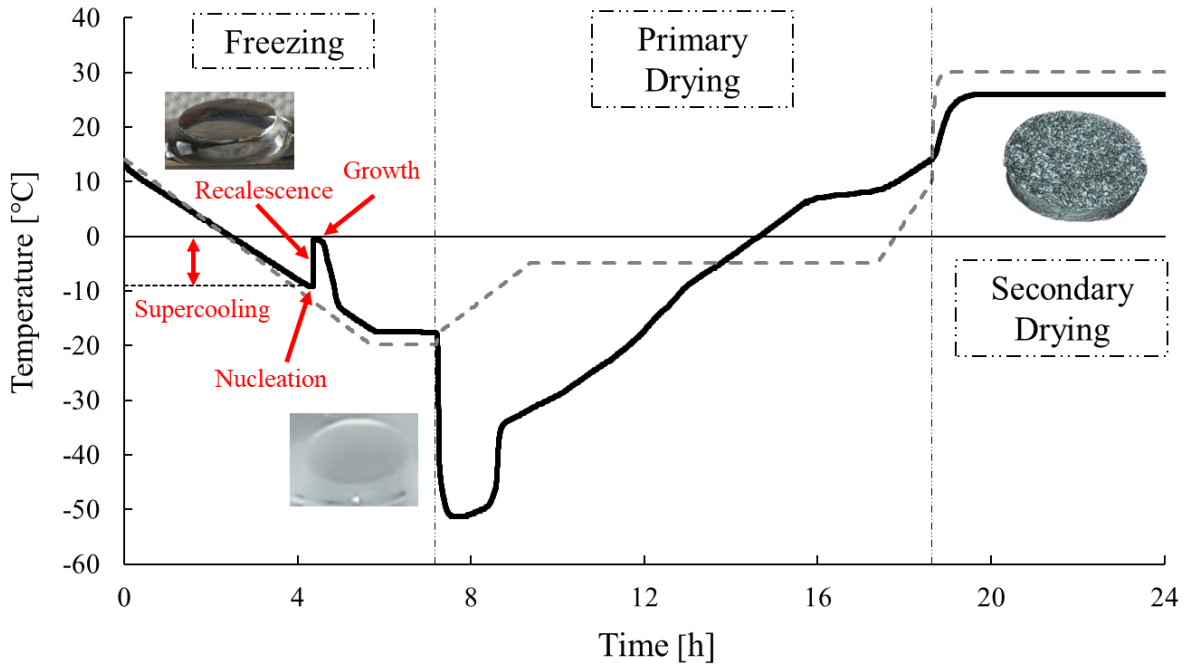
$$\xi = \alpha\left(\overline{r_0^2}\right)^{\frac{1}{2}} \tag{3}$$

where $\boldsymbol{\alpha}$ is the elongation ratio of the polymer chain. Following Canal and Peppas **[31]**, we assumed that the hydrogel is isotropically swollen. $\boldsymbol{\alpha}$ is then related to the swollen polymer volume fraction, $\boldsymbol{v_{2s}}$, by:

$$\boldsymbol{\alpha = v_{2s}^{-\frac{1}{3}}} \tag{4}$$

2.5 Freeze-drying process

Scaffolds (11 mm in diameter, 2 mm in height) swollen in 0.025% NaCl (and drained to remove the solvent excess) were disposed in Petri dishes (VWR, 391-0875) and placed on freeze-dryer trays (MUT 004, Cryotec®). Scaffolds axis was systematically oriented perpendicular to the tray. The freeze-drying protocol consists of three stages (**Fig. 2**). Cooling runs under atmospheric pressure at a constant rate of - 0.1 °C min^{-1} from 15 ˚C to – 20 ˚C followed by a phase at constant temperature of - 20 °C during 90 min. Primary drying occurs at low pressure (0.010 mbar) and - 5 °C for 8 h and secondary drying at 30 °C for 1 hour.



188

189 **Fig. 2**. Freeze-drying of hydrogel scaffolds. The process comprises three stages: freezing,
190 primary drying and secondary drying. Black line: scaffolds temperature; grey dashed line: plate
191 temperature. Here, supercooling is followed by nucleation at – 9 °C.

192

193 ### 2.6 Dedicated nucleation experiments

194 In order to identify the nucleation mechanisms that are in play during freeze-drying, a series of
195 at least 36 independent scaffolds swollen in 0.025% NaCl (10 mm in diameter) were frozen in
196 Petri dishes on freeze-dryer trays (MUT 004, Cryotec®). The scaffolds were separated from
197 each other by no less than two diameters. The constant cooling rate of - 0.2 °C min^{-1} was
198 applied. The number of unfrozen samples, *N(t)* was recorded every minute and associated with
199 the freeze-dryer plate temperature. We then considered that the nucleation temperature of a
200 scaffold coincides with the plate temperature at the onset of its freezing.

201 Moreover, a dedicated cooling protocol was applied on 98 scaffolds according to Vali [32] with
202 - 0.2 °C min^{-1} cooling rate from 15 °C to - 15 °C, then a phase at - 14 °C for 30 minutes and

eventually cooling at - 0.2 °C min^{-1} rate until - 20°C. We determined the variations of the freezing rate, *R*, as a function of time. *R* is defined as the ratio of the number of freezing scaffolds per minute to the number of unfrozen ones [32]. It was derived from the variations of *N*:

$$R(t) = -\frac{N(t+\Delta t) - N(t-\Delta t)}{2\Delta t}\frac{1}{N(t)} \quad (5)$$

with Δt = 2 min.

We found that the exponential function well fits the variations of *R* as a function of time (**Fig. 3B**). Because cooling rate is constant, we deduced that the variations of *R* as a function of temperature may be expressed as

$$R = R(T) = ae^{-bT} \quad (6)$$

Assuming singular hypothesis for nucleation, we determined the so-called differential nucleus concentration, *k(T)*, as defined by Vali [32]. *k(T)* represents the concentration of nuclei per unit volume with activation temperature within one degree. It is then given by

$$k(T) = -\frac{R(T)}{V\,r} \quad (5)$$

where the cooling rate *r* = -0.2°C min^{-1} and the scaffold volume *V* = 0.2 ± 0.02 cm^3.

2.7 Scanning electron microscopy of frozen scaffolds

The scaffolds were collected at the end of cooling stage at - 20°C before primary drying. The samples were stored at - 80 °C until further use. The CamScan Crystal Probe X500FE SEM-EBSD (CNRS UMR 5243, University of Montpellier), equipped with C1001 GATAN gaseous nitrogen cold stage modulus was used to perform the analysis in cold conditions as described previously [22,23]. Briefly, samples preparation was conducted in a freezer at – 60 °C by polishing the surface with cryotome blade just before the analysis. In the chamber, the sample

was maintained between – 90 °C and – 100 °C with 1 Pa vacuum. EBSD was performed with 20 µm step size and 20 Hz acquisition speed concomitantly with EDX. Operating conditions were 20 kV acceleration voltage and 25 mm working distance. Aztec software package from Oxford Instruments HKL was used to index EBSD pattern and align with EDX spectra. Indexation of ice crystal from hexagonal space group 186 with a = 4.51 Å and c = 7.34 Å was successful over more than 90 % of the surface with less than 0.5° angular resolution. Channel5 software package was used to process EBSD patterns into Inverse Pole Figures (IPF) orientation map and pole figures. Ice grains were defined as continuous domains with less than 10° crystallographic misorientation. Ice grain size was defined as the square root of grain area.

2.8 **Porous structure analyses of freeze-dried scaffolds**

The 3D architecture of freeze-dried scaffolds with a voxel size of $(6\ \mu m)^3$ was acquired by X-ray nanotomograph EasyTom XL 150/160 (RX-solutions, France) using a sealed micro-focus tube at a working voltage of 50 kV and a working current of 120 µA. An amorphous silicon matrix plan (ASMP) detector of 1920 × 1536 pixels was used and 1440 radiographs were obtained with an exposure time of 0.2 s and an averaging of 10. The image reconstruction, performed on a server with 4 GPU cards (NVidia GTX1080), requires ca. 2 minutes. By building up the generated 2D slice images, the 3D volume of the sample was achieved using Avizo®.

CLSM (ZEISS LSM700) was used to explore the 3D porous structure of swollen scaffolds labelled with 0.17% (w/w) 500 kDa FITC-dextran (TdB Consultancy) during formulation. After freeze-drying, scaffolds were allowed to swell overnight in 0.025% (w/v) NaCl. XZ views (where Z is the symmetry axis of the scaffold) were acquired over 250-µm depth in 43 confocal slices of 2.5 µm pixel size after cutting the swollen scaffolds with razor blade (0.12HD, ASR). Two-photon microscope (LEICA, SP8) was used to acquire scaffold swollen in DPBS (Gibco, SigmaAldrich) over 250-µm depth in 13 slices with 0.692 µm pixel size.

Pores are defined as objects of air or liquid delimited by dried (or hydrated) cross-linked polysaccharides. Pores were isolated in 3D with Aviso software (Thermo Scientific™) after thresholding, holes filling, object separation (watershed algorithm) and labelling. The pore size was defined as the cubic root of the 3D pore volume. Aviso software provided the geometric orientation of the pores. Polar angle (φ) and azimuthal angle (θ) defined the main axis orientation of an equivalent ellipsoid in 3D for each pore.

2.9 Cell seeding in freeze-dried hydrogel scaffold

MC3T3-E1 pre-osteoblasts cells were cultivated in α-MEM medium with nucleosides without ascorbic acid (GIBCO, A1049001) supplemented with 10% FBS (GIBCO, 10270-106) in standard cell culture conditions. Cell membrane labelling was performed with PKH-26 dye (Phanos Technologies) according to manufacturer protocol. 20 µL of cell suspension (5 10^6 mL^{-1}) was added directly on freeze-dried hydrogel scaffold. Complete swelling was allowed by regular addition of the medium. The scaffolds were then incubated in standard cell culture conditions during 24 h in 6-well plate with 1.5 mL of medium and 4 scaffolds per well. XZ views to 250-µm depth were acquired with CSLM. Hydrogel green signal (FITC dextran) and cell red signal (PKH-26) were recorded on two channels. Cells clusters were analyzed with 3D Object Counter (Fidji, Java Software).

2.10 Statistical methods

Values are given as mean ± standard deviation. Analysis of variance and Student's *t*-test assessed significance of data (Microsoft Excel, 2016). In figures, error bars correspond to standard deviation. Regression analysis was performed with Monte Carlo algorithm (R Core Team, 2016).

3. Results

3.1 Cross-linking and subsequent mesh size of the polysaccharide-based hydrogel

The characteristics of the starting polymers were determined by light scattering measurements, i.e. M_n^{pul} = 158.8 kg mol^{-1}, I_p = 1.98 and R_n = 17.1 ± 0.8 nm for pullulan, and M_n^{dex} = 284.9 kg mol^{-1}, I_p = 1.82 and R_n = 16.0 ± 0.8 nm for dextran. Thus, the number average molecular weight of the 75/25 mixture is M_n = 178.6 kg mol^{-1}. After cross-linking, the volume fraction of the polymer in the relaxed state (i.e. the polymer kept in the solvent used for cross-linking) is equal to v_{2r} = 0.11. Swelling in 0.025% (w/v) NaCl solution results in a swelling volume ratio Q = 80. The volume fraction of the polymer in the swollen state is equal to v_{2s} = 0.012.

Rheological measurements indicate that the hydrogel is incompressible and highly elastic (tan δ = 0.09). At 37 °C in 0.025 % NaCl with frequency of 1 Hz under 0.05% strain and 0.03 N axial force, the storage modulus is estimated at G' = 0.9 ± 0.1 kPa. The average molecular weight between consecutive cross-links, M_c, was determined according to the Gaussian rubber elasticity theory modified by Peppas and Merrill [28], i.e. M_c = 68 kg mol^{-1} for the resulting hydrogel. Under 100% pullulan and 100% dextran assumption, the average molecular weight between consecutive cross-links differs slightly, i.e. $M_c^{pul} = 62$ kg mol^{-1} and $M_c^{dex} = 95$ kg mol^{-1}, respectively. Then, the end-to-end distance of the chains in the unperturbed (solvent-free) state was estimated at $\left(\overline{r_0^2}\right)^{1/2}$ = 19 nm and $\left(\overline{r_0^2}\right)^{1/2}$ = 22 nm, respectively. After swelling in 0.025% NaCl, the mesh size was estimated at ξ = 83 nm and ξ = 94 nm, respectively. We also checked that the chains of the polymer network remain Gaussian: the relative end-to-end distance of the network chains after swelling in 0.025% NaCl is estimated at about 0.2, under 100% pullulan assumption. The relative extension is thus lower than 0.3 corresponding to the onset of deviations from the Gaussian statistics.

We then investigated the fate of the polysaccharide network during and after freeze-drying.

3.2 Nucleation of ice from supercooled hydrogel

Fig. 2 shows that supercooling is followed by nucleation with an abrupt change in opacity during recalescence. Water solidification is achieved close to the ice melting point. In order to characterize the nucleation in the supercooled scaffolds during freeze-drying, series of scaffolds swollen in 0.025% NaCl were cooled at –0.2 °C min^{-1} rate. **Fig. 3A** shows the nucleation temperature histogram with a mean of – 13.3 ± 3 °C well above – 35°C, the homogenous nucleation threshold of pure water [33]. The nucleation is therefore heterogeneous. Heterogeneous nucleation of ice from supercooled water is known to be influenced by two factors, i.e. the properties of the nucleating sites and the growth of embryo to critical size by the random fluctuations [34]. When the former is predominant, nucleation is said to be singular [35]. When the latter prevails, nucleation is stochastic and the classic nucleation theory (CNT) applies. A series of 98 scaffolds was cooled according to the time-temperature pattern similar to Vali [32] in order to discriminate the predominant factor. **Fig. 3B** represents the variations of the freezing rate as a function of time. While temperature decreases for 30 minutes from -9°C to -15°C, 36.7% of scaffolds freeze, and freezing rate increases exponentially with time (slope of the log-linear plot equal to 0.076 ± 0.008 min^{-1}, R-squared = 0.91). Then, from -14°C to -20°C, 44.9% of scaffolds freeze, and freezing rate increases exponentially with about the same slope (0.1 ± 0.01 min^{-1}, R-squared = 0.87). Since the temperature varies linearly with time, we may deduce the differential nucleus concentration, i.e. $k(T) \cong (3 \times 10^{-4} \pm 2 \times 10^{-4}) \exp[-(0.38 \pm 0.04)T]$ nuclei cm^{-3} $°C^{-1}$ valid for $T \in [-9°C; -15°C]$. This estimate is close to that reported by Vali for water drops [32]. While temperature is kept constant at – 14 °C for 30 minutes, only 5 frozen events occur (5%) even if a large fraction of the scaffolds is still unfrozen. It means that most of the nucleating sites with characteristic temperature higher than -14°C have already induced a nucleation event during cooling from -9°C to -15°C. Thus, there is a depletion of active sites

with characteristic temperature close to the plateau temperature (-14°C) and freezing rate is drastically reduced. This behavior is characteristic of the singular model and cannot be explained by the CNT.

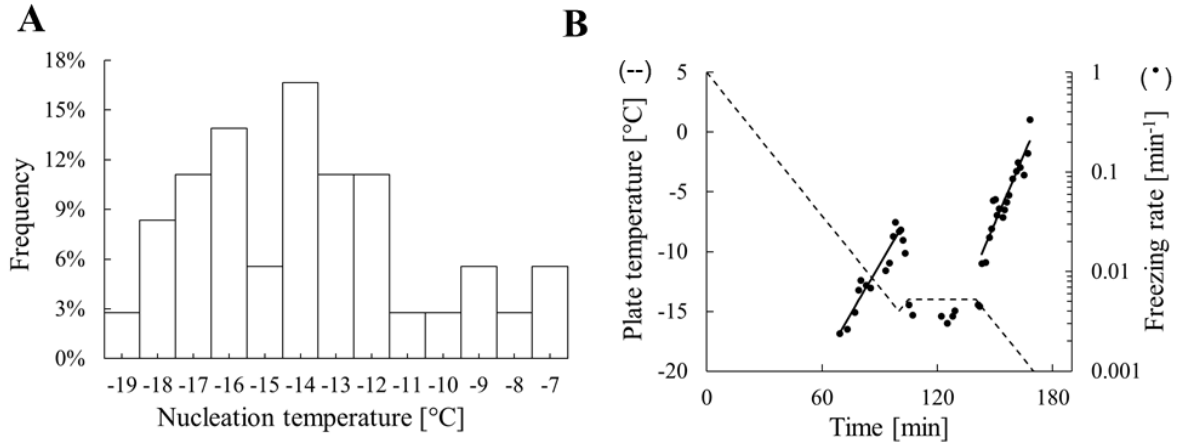


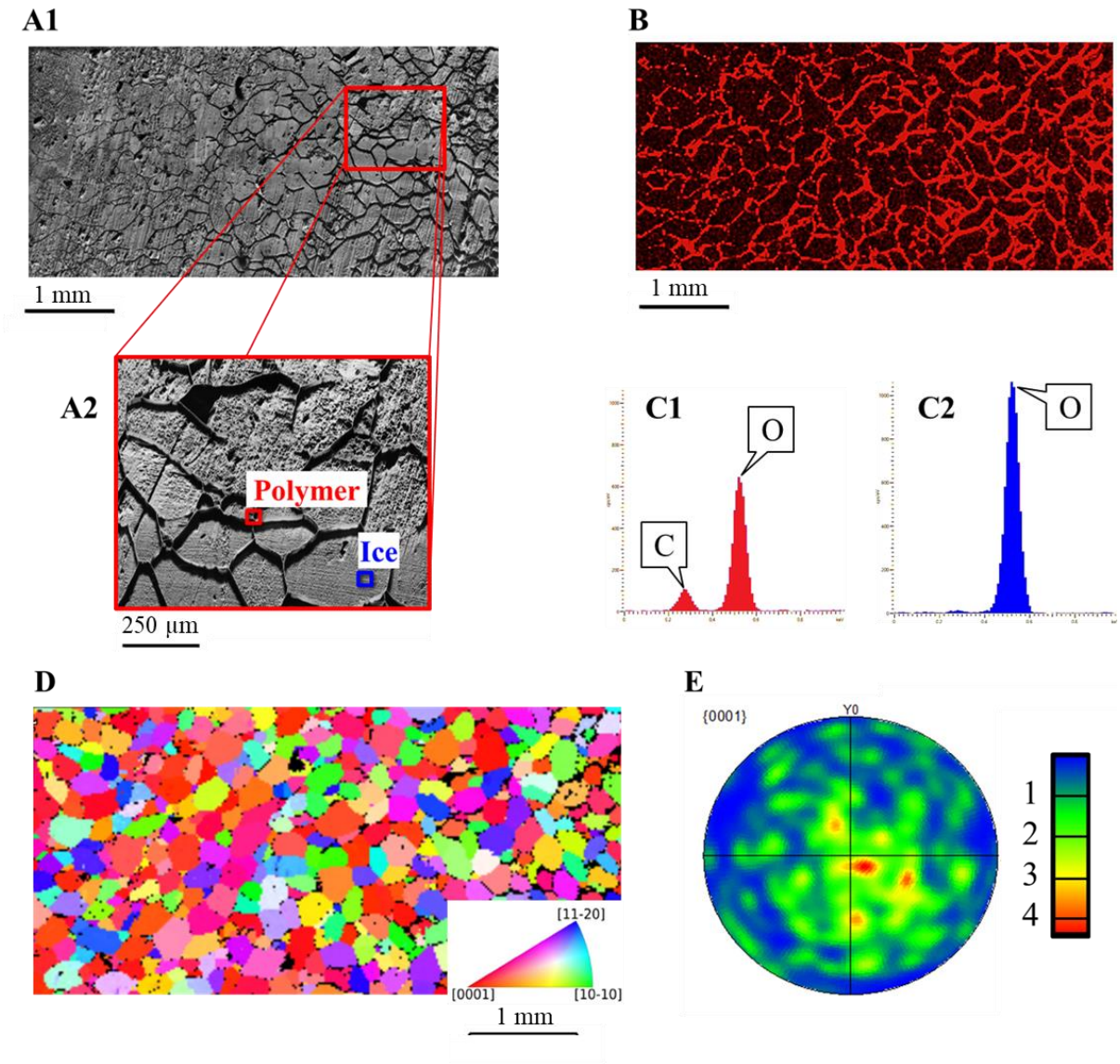
Fig. 3 Characterization of ice nucleation within scaffolds preliminary swollen in 0.025% NaCl and submitted to a dedicated cooling protocol. **A**: Histogram of nucleation temperature for a batch of 36 scaffolds cooled at – 0.2 °C min^{-1}. **B**: Semi-log plot of the freezing rate of a batch of 98 scaffolds submitted to a time-temperature pattern similar to Vali [32]: cooling from 5°C to -15°C at – 0.2 °C min^{-1}, plateau at -14°C during 30 minutes and cooling from -14°C to -20°C at – 0.2 °C min^{-1}.

Following nucleation, ice growth takes place in two stages, i.e. the initial rapid recalescent stage and the final slower stage close the ice melting point, T_m [36]. During recalescence, the ice structure appears as a "milky-white cloud" expanding with a velocity of 6.5 ± 3.5 cm s^{-1} in line with findings on water drops [36,37]. Recalescence ends when scaffold temperature reaches T_m (temperature increase due to latent heat release). The fraction of frozen water is then estimated at $c_p(T_m - T_n)/L \cong 9\%$ where c_p is the heat capacity of water, L the heat of fusion and T_n the nucleation temperature. Freezing is completed at the end of the slower stage.

3.3 **Polycrystalline structure of the frozen hydrogel scaffolds**

Scanning electron microscopy was performed at – 100 °C to prevent samples from quick sublimation. An XY cross-section of a frozen scaffold (nucleation temperature of - 9.7 °C**)** is shown with topographic contrast on **Fig. 4A**: flat regions of about 200 µm in length are surrounded by ridges. The elemental map of **Fig. 4B** shows that carbon is mainly located in the ridges. EDX spectra of a flat region (labelled "ice") and a ridge (labelled "polymer") further evidenced carbon in the "polymer" region (**Fig. 4C1**), while no significant signal was recorded for the "ice" region (**Fig. 4C2**). These topographic and chemical analysis prove that the ice domains are surrounded by polysaccharide. Topography was due to the slight sublimation of ice under the vacuum of the microscope even at – 100 °C.

EBSD, performed with an Oxford Instruments NordlysNano EBSD detector, was used to examine the microstructure of the frozen scaffold. Crystal orientation map is displayed in the so-called Inverse Pole Figure (IPF). In this IPF, ice grains are labelled according to the measured orientation with respect to the reference direction that is parallel to the scaffold Z axis (**Fig. 4D**). EBSD data show that water solidified into hexagonal (Ih) ice. Ice is polycrystalline with an average grain size over 4 preparations found to be 160 ± 20 µm. Grains have equiaxed morphology and texture. However, c-axis pole figure. shows that the highest pole densities are obtained in and around Z, i.e., at the central region of the pole figure. (**Fig. 4E**). Thus, Ih-ice c-axis is preferentially parallel to Z.



359

360 **Fig. 4**. Scanning electron microscopy at -100°C of a frozen scaffold horizontal cross-section.
361 **A1**: Topography contrast. **A2**: Zoom and definition of labelled areas. **B**: Carbon map obtained
362 by EDX. **C1** and **C2**: EDX spectra of the labelled areas "polymer" and "ice", respectively. **D**:
363 Z-direction IPF coloring orientation map obtained via EBSD (20 µm step size) and associated
364 IPF key. Red color corresponds to Ih-ice grains with c-axis ([0001]) parallel to Z-direction. **E**:
365 c-axis pole figure.

3.4 **3D porous structure of freeze-dried scaffold**

The 3D porous structure of an entire scaffold was analyzed by X-ray computed tomography with $(6\ \mu m)^3$ voxel size (**Fig. 5A**). A highly porous structure with very thin walls was observed similarly to previously reported micro-computed tomography analysis of freeze-dried gels [38]. After image processing, the porosity was estimated at $\varepsilon = 93\% \pm 2\%$ and mean pore size at 280 ± 20 µm. About 6% of the pores are micropores (<100µm) and 94% are macropores (>100µm) according to standard nomenclature [39].

The distribution of azimuthal and radial orientations of pore major axis indicates that major axis is preferred parallel to XY plane (distribution of φ maximal close to 90°) without preferential orientation in the XY plane (uniform distribution of θ) (**Fig. 5B**).

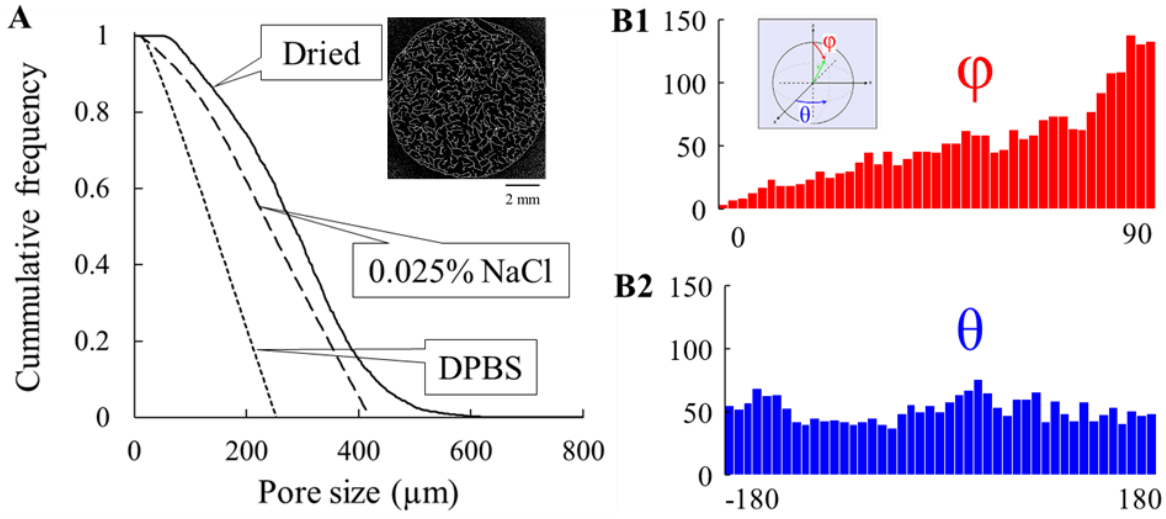
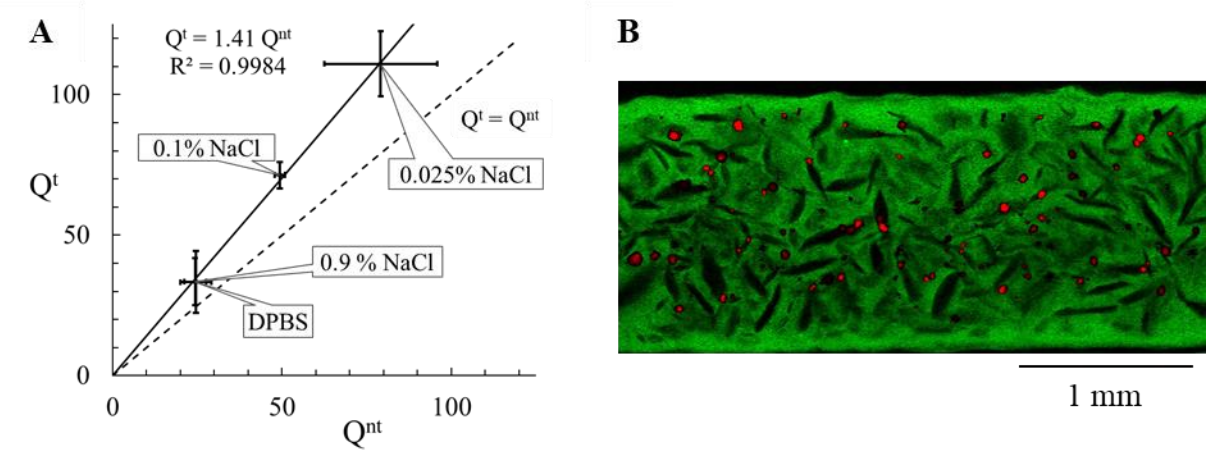


Fig. 5. 3D assessment of the freeze-dried scaffold porosity. **A**: Pore size cumulative distribution of an entire scaffold (9.36 mm in diameter, 1.73 mm in height) after freeze-drying (solid line); scaffolds analyzed to 250-µm depth after swelling in 0.025% NaCl (dash line) and in DPBS (dotted line). XY slice at 500 µm depth of the X-ray tomography scan with $(6\ \mu m)^3$ voxel size. **B1** and **B2**: Distribution of polar (φ) and azimuthal (θ) angles of pore major axis, in the dried scaffold.

3.5 **Hydrogel porous structure after swelling**

Hydrogel swelling was investigated for a series of solvents of increasing ionic strength, i.e. 0.025% NaCl, 0.1% NaCl, 0.9% NaCl and Dulbecco's Phosphate Buffer Saline solution (DPBS) used for cell culture. For each solvent, the swelling volume ratio (Q) was determined for the textured hydrogel (resp. non-textured, i.e. non freeze-dried). **Fig. 6A** shows that for both textured and non-textured hydrogels, the swelling volume ratio increases as the solvent ionic strength decreases. This is consistent with the anionic nature of the grafted phosphate [40]. The swelling ratio of the textured hydrogel, Q^t, is greater than the swelling ratio of the non-textured hydrogel, Q^{nt}. We found that Q^t varies linearly with Q^{nt}. Since the porosity is given by $\varepsilon = 1 - (Q^{nt}/Q^t)$, we deduce that the porosity of the textured hydrogel in the swollen state is constant for the tested solvent series and equal to $\varepsilon = 29\% \pm 2\%$. Correlatively the pore network varies homothetically when changing solvent.

We further investigated the 3D porous structure of textured hydrogels prepared using FITC-dextran after swelling in 0.025% NaCl solution using CLSM. The volume of interest was a slab parallel to Z of 250 µm-thickness. The porosity measured by image analysis was equal to $\varepsilon = 29\%$. After pore separation procedure, the mean pore size was estimated at 120 µm. We can conclude that swelling in 0.025 NaCl% results in pores collapse with the pore size 2.3 times smaller than in the dry state. After swelling in DPBS, textured hydrogel was investigated using two-photon excitation laser scanning microscopy to minimize scattering in the hydrogel. The porosity was estimated at $\varepsilon = 30\%$ and the mean pore size at 54 µm. We thus found that pore size varies by a scale factor of 2.2 between DPBS and 0.025% NaCl solution, a value consistent with the scale factor deduced from swelling volume ratio measurements, i.e. $3.3^{1/3} \cong 1.5$.



406

407 **Fig. 6.** Fate of the porous structure after swelling and 3D cell culture.
408 **A**: Swelling volume ratio for textured (Q_t) and non-textured (Q_{nt}) scaffolds swollen in 0.025%
409 NaCl, 0.1% NaCl, 0.9% NaCl and DBPS. The linear regression model is fitted to the data
410 without the intercept term. **B**: CLSM XZ cross-section of a freeze-dried scaffold (7.2 mm
411 diameter, 1.4 mm height) 24 h after the seeding of 100,000 MC3T3-E1 cells.

412

413 ### 3.6 Cell seeding demonstrates interconnectivity of pores

414 Dry textured scaffolds were seeded with 100,000 MC3T3-E1 cells previously labelled with
415 PKH-26. Clusters were observed 24 h after seeding in the pores, homogenously distributed on
416 the scaffold volume (observation to 300-µm depth of entire XY sections, see **Fig. 6B** for one
417 XZ slice). Our results demonstrate that the pores in the freeze-dried scaffold are adequately
418 interconnected to allow homogenous cell distribution. Mean cluster volume was 81×10^{-3}
419 μm^3 corresponding to aggregates of 27 cells in average according to mean MC3T3-E1 volume
420 [41]. Interestingly, cluster diameter (53 µm) was close to mean pore size (54 µm) which
421 suggests that cells organized according to the scaffold porous structure.

422

4. Discussion

Scaffold freezing is initiated at significant supercooling (about 13°C) by heterogeneous nucleation. The sites are likely located at the interface between the hydrogel and the plate or on the polymer network [34]. We found that the heterogeneous nucleation is singular (**Fig. 3B**). Very few nucleating sites are present in each scaffold (about 0.1 nuclei cm^{-3} $°C^{-1}$ estimated at -15°C). During cooling, freezing is triggered by the nucleating site with the highest characteristic temperature, and the scaffold freezing temperature is equal to the characteristic temperature of this site [32]. At this temperature, the time needed for an embryo to reach the critical size is much lower than the cooling characteristic time (instantaneous embryo growth). Consistently, in a batch of scaffolds, the number of freezing scaffolds per temperature interval is expected to be almost independent of the cooling rate.

At the onset of freezing, growing ice crystals are expected to be needle-like for the present supercooling values [42]. These needles exhibit a tree-like structure called needled branch [42]. We hypothesized that the rapid growth during the recalescent stage was accompanied by fragmentation of these needles due to the constraints exerted by the surrounding nano-scale polymer network. The fragments induces secondary nucleation [43] and the subsequent equiaxed polycrystalline structure observed on the frozen scaffold with EBSD (**Fig. 4D**). Most ice grains are formed from secondary nucleation. Since the solubility of the polymer is lower in ice than in liquid water, the polymer chains are rejected by the growing ice crystals into the intergranular space and form a macro-network. Simultaneous EDX and EBSD analyses show that each pore results from the growth of one to a few ice crystals. Since the mesh size of the polymer network (about 90 nm) is several orders of magnitude lower than the ice grain size (about 160 µm), polymer exclusion is accompanied by massive chain reorganizations and may be also by some ruptures of chains or cross-links. X-ray tomography of freeze-dried scaffolds

showed that the polymer network remains continuous. Since cell seeding demonstrated that the pores of the freeze-dried scaffolds are interconnected, we conclude that in the frozen scaffolds, the polymer macro-network and the ice network are interlaced on the ice grain scale.

In perfect equiaxed growth, random orientation of the ice crystals within the scaffold is expected [36]. However, EBSD analysis (**Fig. 4E**) shows that the c-axis pole densities are higher in Z-direction. We infer that this preferred orientation is induced from the scaffold bottom. Indeed, needled branch crystals (as snow crystals) are substantially planar with c-axis orthogonal to that plane since growth kinetics in the basal plane is much larger than in c-axis direction [44]. Needled branch crystals which are parallel to the supporting plate (XY plane) are in the best thermal conditions to increase in thickness [34], which explains the observed anisotropy. Paradoxically, this preferred orientation (parallel to Z) is consistent with the preferential orientation of the pore, i.e. major axis parallel to XY plane, since growth is faster in the basal plane which presently coincides with XY plane.

The porosity decreases significantly between freeze-dried and swollen states, i.e. from $\varepsilon = 93 \pm 2\%$ down to $\varepsilon = 29\% \pm 2\%$. In the swollen state, the hydrogel porosity remains constant when increasing the solvent ionic strength even if the pores shrink. This remarkable result was confirmed by CLSM and two-photon microscopy of scaffolds prepared with FTIC-dextran.

A homogenous seeding of MC3T3-E1 cells within the pore network was achieved by the simple addition of a cell suspension on freeze-dried scaffolds. Isolated cells of different origins (species, tissues), two or more cell types, or cell clusters can be accommodated in these 3D porous scaffolds [17–19,21]. Such scaffolds are suitable for cell culture in 3D (especially when cell clustering and spheroid growth is necessary for studying cell development and differentiation), for tissue engineering or for pharmacological assays in 3D.

5. Conclusions

This study presented the mechanisms of pore formation during the freeze-drying of a cross-linked hydrogel at a low cooling rate and highlighted the interactions between the nano-scale polymer network and the growing ice crystals. We demonstrated the strong link between pore formation and the nucleation of ice.

The primary nucleation, heterogeneous and singular, occurs at significant supercooling. During recalescence, the rapidly growing ice needles fracture due to the constraints exerted by the surrounding nano-scale polymer network. The needle fragments induce secondary nucleation and a subsequent fine-grained polycrystalline structure. As freezing continues close to the ice melting point, the ice crystals get bigger, and reject the polymer in the intergranular space. Electron cryo-microscopy actually showed that the polymer chains segregate on the ice grain boundary network and form a macro-network. The characteristic length scale of the macro-network coincides with the ice grain size (160 µm) and is several orders of magnitude greater than the macromolecular correlation length (90 nm). Despite the scale separation between the mesh size and the ice grain size, we expect that a lower mesh size (obtained with a greater degree of cross-linking) should result in a lower grain size (and smaller macro-pores) since the secondary nucleation of ice would be enhanced.

After sublimation, ice grains are replaced by macro-pores (280 µm mean size as measured by high-resolution X-ray tomography). The resulting dry structure is highly porous (93%). In the swollen state, the porosity decreases down to 29%. When the solvent ionic strength increases, the pores shrink (120 µm in 0.025% NaCl and 54 µm in DBPS) whereas the porosity remains constant. This remarkable result was confirmed by CLSM and two-photon microscopy. The scaffolds were further validated with the culture of pre-osteoblastic cells: the pores in the freeze-dried scaffold are adequately interconnected to allow homogenous cell seeding.

These findings should guide the strategies implemented to control the porous structure of hydrogel scaffolds.

Acknowledgements

This work is supported by the "IDI 2016" project funded by the IDEX Paris-Saclay, ANR-11-IDEX-0003-02. The authors acknowledge the 3D-BioMat project that is co-financed by the Grand Reims and the European Union with a total budget of 965,000€, hosted by the CEBB (51110 Pomacle, France) from 01/05/2016 to 30/04/2019. The authors acknowledge Dr Marie-Noëlle Labour and Cyril Breton for their kind help with two-photon microscopy and confocal microscopy, respectively. The authors acknowledge Isabelle Bataille for her help with the rheometer and Soraya Lanouar for the chemical characterizations of polymer batches.

Conflict of Interest

The authors declare that they have no conflict of interest.

References

[1] J.L. Drury, D.J. Mooney, Hydrogels for tissue engineering: scaffold design variables and applications, Biomaterials. 24 (2003) 4337–4351. doi:10.1016/S0142-9612(03)00340-5.

[2] I.V. Yannas, J.F. Burke, P.L. Gordon, C. Huang, R.H. Rubenstein, Design of an artificial skin. II. Control of chemical composition, J. Biomed. Mater. Res. 14 (1980) 107–132. doi:10.1002/jbm.820140203.

[3] F.J. O'Brien, B.A. Harley, I.V. Yannas, L.J. Gibson, The effect of pore size on cell adhesion in collagen-GAG scaffolds, Biomaterials. 26 (2005) 433–441. doi:10.1016/j.biomaterials.2004.02.052.

[4] J.J. Campbell, A. Husmann, R.D. Hume, C.J. Watson, R.E. Cameron, Development of three-dimensional collagen scaffolds with controlled architecture for cell migration studies using breast cancer cell lines, Biomaterials. 114 (2017) 34–43. doi:10.1016/j.biomaterials.2016.10.048.

[5] E. Sachlos, J. Czernuszka, Making Tissue Engineering Scaffolds Work. Review: The application of solid freeform fabrication technology to the production of tissue engineering scaffolds, Eur. Cell. Mater. 5 (2003) 29–40. doi:10.22203/eCM.v005a03.

[6] L. Qian, H. Zhang, Controlled freezing and freeze drying: a versatile route for porous and micro-/nano-structured materials, J. Chem. Technol. Biotechnol. 86 (2011) 172–184. doi:10.1002/jctb.2495.

[7] N. Dagalakis, J. Flink, P. Stasikelis, J.F. Burke, I.V. Yannas, Design of an artificial skin. Part III. Control of pore structure, J. Biomed. Mater. Res. 14 (1980) 511–528.
[8] H. Yoshida, T. Hatakeyama, H. Hatakeyama, Characterization of water in polysaccharide hydrogels by DSC, J. Therm. Anal. 40 (1993) 483–489. doi:10.1007/BF02546617.
[9] F. O'Brien, Influence of freezing rate on pore structure in freeze-dried collagen-GAG scaffolds, Biomaterials. 25 (2004) 1077–1086. doi:10.1016/S0142-9612(03)00630-6.
[10] H.-W. Kang, Y. Tabata, Y. Ikada, Fabrication of porous gelatin scaffolds for tissue engineering, Biomaterials. 20 (1999) 1339–1344. doi:10.1016/S0142-9612(99)00036-8.
[11] H. Zhang, I. Hussain, M. Brust, M.F. Butler, S.P. Rannard, A.I. Cooper, Aligned two- and three-dimensional structures by directional freezing of polymers and nanoparticles, Nat. Mater. 4 (2005) 787–793. doi:10.1038/nmat1487.
[12] H. Zhang, A.I. Cooper, Aligned Porous Structures by Directional Freezing, Adv. Mater. 19 (2007) 1529–1533. doi:10.1002/adma.200700154.
[13] C.R. Rowland, L.A. Colucci, F. Guilak, Fabrication of anatomically-shaped cartilage constructs using decellularized cartilage-derived matrix scaffolds, Biomaterials. 91 (2016) 57–72. doi:10.1016/j.biomaterials.2016.03.012.
[14] S. Deville, Freezing as a Path to Build Complex Composites, Science. 311 (2006) 515–518. doi:10.1126/science.1120937.
[15] T.M. Freyman, I.V. Yannas, L.J. Gibson, Cellular materials as porous scaffolds for tissue engineering, Prog. Mater. Sci. 46 (2001) 273–282. doi:10.1016/S0079-6425(00)00018-9.
[16] J.C. Fricain, S. Schlaubitz, C. Le Visage, I. Arnault, S.M. Derkaoui, R. Siadous, S. Catros, C. Lalande, R. Bareille, M. Renard, T. Fabre, S. Cornet, M. Durand, A. Léonard, N. Sahraoui, D. Letourneur, J. Amédée, A nano-hydroxyapatite – Pullulan/dextran polysaccharide composite macroporous material for bone tissue engineering, Biomaterials. 34 (2013) 2947–2959. doi:10.1016/j.biomaterials.2013.01.049.
[17] C. Ehret, R. Aid-Launais, T. Sagardoy, R. Siadous, R. Bareille, S. Rey, S. Pechev, L. Etienne, J. Kalisky, E. de Mones, D. Letourneur, J. Amedee Vilamitjana, Strontium-doped hydroxyapatite polysaccharide materials effect on ectopic bone formation, PLOS ONE. 12 (2017) e0184663. doi:10.1371/journal.pone.0184663.
[18] J.C. Fricain, R. Aid, S. Lanouar, D.B. Maurel, D. Le Nihouannen, S. Delmond, D. Letourneur, J. Amedee Vilamitjana, S. Catros, In-vitro and in-vivo design and validation of an injectable polysaccharide-hydroxyapatite composite material for sinus floor augmentation, Dent. Mater. 34 (2018) 1024–1035. doi:10.1016/j.dental.2018.03.021.
[19] J. Guerrero, H. Oliveira, R. Aid, R. Bareille, R. Siadous, D. Letourneur, Y. Mao, J. Kohn, J. Amédée, Influence of the three-dimensional culture of human bone marrow mesenchymal stromal cells within a macroporous polysaccharides scaffold on Pannexin 1 and Pannexin 3, J. Tissue Eng. Regen. Med. 12 (2018) e1936–e1949. doi:10.1002/term.2625.
[20] S. Lanouar, R. Aid-Launais, A. Oliveira, L. Bidault, B. Closs, M.-N. Labour, D. Letourneur, Effect of cross-linking on the physicochemical and in vitro properties of pullulan/dextran microbeads, J. Mater. Sci. Mater. Med. 29 (2018). doi:10.1007/s10856-018-6085-x.
[21] E.J. Ribot, C. Tournier, R. Aid-Launais, N. Koonjoo, H. Oliveira, A.J. Trotier, S. Rey, D. Wecker, D. Letourneur, J. Amedee Vilamitjana, S. Miraux, 3D anatomical and perfusion MRI for longitudinal evaluation of biomaterials for bone regeneration of femoral bone defect in rats, Sci. Rep. 7 (2017) 6100. doi:10.1038/s41598-017-06258-0.
[22] S. Piazolo, M. Montagnat, J.R. Blackford, Sub-structure characterization of experimentally and naturally deformed ice using cryo-EBSD, J. Microsc. 230 (2008) 509–519. doi:10.1111/j.1365-2818.2008.02014.x.

[23] M. Montagnat, T. Chauve, F. Barou, A. Tommasi, B. Beausir, C. Fressengeas, Analysis of Dynamic Recrystallization of Ice from EBSD Orientation Mapping, Front. Earth Sci. 3 (2015) 81. doi:10.3389/feart.2015.00081.
[24] A. Autissier, C.L. Visage, C. Pouzet, F. Chaubet, D. Letourneur, Fabrication of porous polysaccharide-based scaffolds using a combined freeze-drying/cross-linking process, Acta Biomater. 6 (2010) 3640–3648. doi:10.1016/j.actbio.2010.03.004.
[25] D. İmren, M. Gümüşderelioğlu, A. Güner, Synthesis and characterization of dextran hydrogels prepared with chlor- and nitrogen-containing crosslinkers, J. Appl. Polym. Sci. 102 (2006) 4213–4221. doi:10.1002/app.24670.
[26] K. Nishinari, K. Kohyama, P.A. Williams, G.O. Phillips, W. Burchard, K. Ogino, Solution properties of pullulan, Macromolecules. 24 (1991) 5590–5593. doi:10.1021/ma00020a017.
[27] K. Kendall, Molecular Adhesion and Its Applications: the Sticky Universe, Springer US, Boston, MA, 2004. http://public.eblib.com/choice/publicfullrecord.aspx?p=3036018 (accessed August 31, 2018).
[28] L.R.G. Treloar, The Physics of rubber elasticity, Clarendon Press, Oxford, 2005. http://www.myilibrary.com?id=134637 (accessed January 10, 2019).
[29] N.A. Peppas, E.W. Merrill, Crosslinked poly(vinyl alcohol) hydrogels as swollen elastic networks, J. Appl. Polym. Sci. 21 (1977) 1763–1770. doi:10.1002/app.1977.070210704.
[30] G.S. Buliga, D.A. Brant, Temperature and molecular weight dependence of the unperturbed dimensions of aqueous pullulan, Int. J. Biol. Macromol. 9 (1987) 71–76. doi:10.1016/0141-8130(87)90029-8.
[31] T. Canal, N.A. Peppas, Correlation between mesh size and equilibrium degree of swelling of polymeric networks, J. Biomed. Mater. Res. 23 (1989) 1183–1193. doi:10.1002/jbm.820231007.
[32] G. Vali, Freezing Rate Due to Heterogeneous Nucleation, J. Atmospheric Sci. 51 (1994) 1843–1856. doi:10.1175/1520-0469(1994)051<1843:FRDTHN>2.0.CO;2.
[33] H.R. Pruppacher, J.D. Klett, Microphysics of Clouds and Precipitation, Nature. 284 (1980) 88–88. doi:10.1038/284088b0.
[34] P.V. Hobbs, Ice physics, Oxford, Clarendon Press, 1974.
[35] G. Vali, Repeatability and randomness in heterogeneous freezing nucleation, Atmospheric Chem. Phys. 8 (2008) 5017–5031.
[36] M. Schremb, C. Tropea, Solidification of supercooled water in the vicinity of a solid wall, Phys. Rev. E. 94 (2016) 052804. doi:10.1103/PhysRevE.94.052804.
[37] S.V. Alekseenko, C. Mendig, M. Schulz, M. Sinapius, O.A. Prykhodko, An experimental study of freezing of supercooled water droplet on solid surface, Tech. Phys. Lett. 42 (2016) 524–527. doi:10.1134/S1063785016050187.
[38] M. Cassanelli, I. Norton, T. Mills, Role of gellan gum microstructure in freeze drying and rehydration mechanisms, Food Hydrocoll. 75 (2018) 51–61. doi:10.1016/j.foodhyd.2017.09.013.
[39] ASTM F2450-18, Standard Guide for Assessing Microstructure of Polymeric Scaffolds for Use in Tissue-Engineered Medical Products, ASTM International, 2018. doi:10.1520/F2450-18.
[40] A. Fernández-Nieves, A. Fernández-Barbero, F.J. de las Nieves, Salt effects over the swelling of ionized mesoscopic gels, J. Chem. Phys. 115 (2001) 7644–7649. doi:10.1063/1.1403002.
[41] L. Klembt Andersen, S. Antoranz Contera, J. Justesen, M. Duch, O. Hansen, J. Chevallier, M. Foss, F. Pedersen, F. Besenbacher, Cell volume increase in murine MC3T3-E1 pre-osteoblasts attaching onto biocompatible Tantalum observed by magnetic AC mode

Atomic Force Microscopy, Eur. Cell. Mater. 10 (2005) 61–69. doi:10.22203/eCM.v010a07.
[42] A.A. Shibkov, Yu.I. Golovin, M.A. Zheltov, A.A. Korolev, A.A. Leonov, Morphology diagram of nonequilibrium patterns of ice crystals growing in supercooled water, Phys. Stat. Mech. Its Appl. 319 (2003) 65–79. doi:10.1016/S0378-4371(02)01517-0.
[43] S.G. Agrawal, A.H.J. Paterson, Secondary Nucleation: Mechanisms and Models, Chem. Eng. Commun. 202 (2015) 698–706. doi:10.1080/00986445.2014.969369.
[44] H. Nada, Y. Furukawa, Anisotropy in growth kinetics at interfaces between proton-disordered hexagonal ice and water: A molecular dynamics study using the six-site model of H2O, J. Cryst. Growth. 283 (2005) 242–256. doi:10.1016/j.jcrysgro.2005.05.057.